IEEE Access
Multidisciplinary | Rapid Review | Open Access Journal

Received December 20, 2021, accepted January 12, 2022, date of publication January 18, 2022, date of current version January 27, 2022.

Digital Object Identifier 10.1109/ACCESS.2022.3144600

Real Time Simulation of Brushless Doubly Fed Reluctance Generator Driven Wind Turbine Considering Iron Saturation

EMAD F. YASSIN, HAITHAM M. YASSIN, AHMED HEMEIDA, AND MOHAB M. HALLOUDA
Electrical Power Engineering Department, Faculty of Engineering, Cairo University, Giza 12613, Egypt
Corresponding author: Emad F. Yassin (emadfathy@eng.cu.edu.eg)

ABSTRACT Brushless doubly fed reluctance generator (BDFRG) provides a good substitute for the doubly fed induction generator for the wind energy applications due to the nonexistence of the slip rings. Real time modelling of the BDFRG is a challenge due to the high leakage inductance of the stator windings. While the magnetic saturation of the iron parts affects the inductances values, therefore studying the effect of magnetic saturation on the BDFRG performance is important. In this paper, a BDFRG model including iron saturation is built. The finite element (FE) analysis using FEMM software is used to generate the relationship between the generator currents and the inductances, the generated data are recorded in a lookup table. A Simulink model of the BDFRG driven wind turbine, with two cases of constant and variable inductances, are developed and verified with FE analyses at range of wind speeds above and below the synchronous speed. The lookup table proposes is verified using finite element analysis at different modes of operation of wind speed and compared with the constant inductance model to show the importance of saturation inclusion in the generator model for accurate generator modelling representation.

INDEX TERMS Brushless doubly fed reluctance generator, analytical model, finite element model, wind turbine.

ABBREVIATIONS

BDFRG	Broushless doubly fed reluctance generator
DFIG	Doubly fed induction generator
GSC	Grid side converter
MSC	Machine side converter
PWM	Pulse width modulation
FE	Finite element
FEMM	Finite element method magnetics
LVRT	Low voltage ride through
MECs	Magnetic equivalent circuits
EC	Electric circuit
FOC	Field oriented control
MTPA	Maximum torque per secondary current
PI	Proportional integral controller
PLL	Phase locked loop
4-D	4 dimensional

NOMENCLATURE

GENERATOR

v, i, λ	Voltage, current and induced flux
α_p, α_s	Primary and secondary current angles
L_p, L_s	Primary and secondary inductances
L_{ps}	Mutual inductance
p_p, p_s	Pair poles of primary and secondary winding
p_r	Rotor poles or sectors
R_p, R_s	Primary and secondary phase resistance
ω_p, ω_s	Primary and secondary electrical angular velocities
ω_r,ω_{rm}	Electrical and mechanical rotor angular velocities
θ_r, θ_{rm}	Electrical and mechanical rotor position
J_m	Moment of inertia
P_p	Primary active power
Q_p	Primary reactive power
T_e	Electromagnetic torque

SUBSCRIPTS

pd, pq	Direct and quadrature primary component
sd, sq	Direct and quadrature secondary component

TURBINE

β	Blade pitch angle
ρ	Air density

The associate editor coordinating the review of this manuscript and approving it for publication was Anamika Dubey.

C_p	Wind power coefficient
P_{mw}	Mechanical power
R	Turbine blade radius
u_w	Wind speed
λ_t	Tip-speed ratio
λ_{opt}	Optimum tip-speed ratio

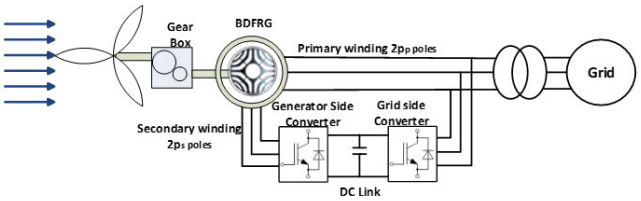

FIGURE 1. Block structure of variable wind speed topology using BDFRG.

I. INTRODUCTION

The interest of using the brushless doubly fed reluctance generator (BDFRG) in wind power applications is remarkably increased in the recent years due to high efficiency, low maintenance and brushless rotor structure. The advantages of BDFRG compered to counterparts makes it a robust and reliable candidate to be used in variable speed wind applications [1]. The BDFRG stator consists of two sets of three phase windings, primary and secondary windings. In wind energy system, the primary winding (grid winding) connected directly to the grid and the secondary winding (control winding) connected to the grid through a partial scale (AC/DC/AC) converter, as shown in Fig 1.

The number of poles of each stator set are different, and the rotor is a reluctance type. The coupling between the two stator windings depends on the presence of rotor saliency. Moreover, the rotor has poles p_r equal to half the summation of the two stator poles to ensure the mutual coupling between the two stator windings [2]–[4] (i.e. $p_r = p_p + p_s$ where, p_p, p_s are the pair poles of the primary and secondary winding respectively).

The BDFRG is similar in operation with doubly fed induction generator (DFIG) and use partial scale converter with variable speeds, moreover, the brushless construction increases the system reliability and compatibility. BDFRG is more efficient when compared with DFIG with the same stator size due to the absence of rotor winding [5]. Thanks to the high leakage inductance of the BDFRG stator windings, increases the capability of low voltage ride through (LVRT) without needing a crow-bar security comparing with DFIG [6].

From published materials in literature, the BDFRG is usually modelled with the assumption of linear inductance, although in nominal operation, the iron nonlinearity is observed. The iron nonlinearites are considered as a key issue, which directly affect the generator torque and control performance.

A detailed model for the saturation is required for a precise control of BDFRG, besides studying the generator peak power under limitations enforced by saturation.

The generator electromagnetic torque is directly dependent on the generator inductances, on the other side, the generator inductances vary with load currents as a consequence of iron saturation [7]. Furthermore, the control performance is highly affected by the direct and quadrature currents which depend on the inductance saturation [8], Therefore, adjusting invariable values for the generator inductances is not adequate for a detailed BDFRG control modelling.

For BDFRG accurate modelling, several solutions exist in literature [9]–[15], models are classified to either electromagnetic field analysis or electric circuit-based models [9], [10]. For the electromagnetic field analysis, the BDFRG can be modelled using finite element (FE) analysis considering all the non-linearities of the soft magnetic material [1], [11]. The model in this case is accurate compared to experimental results. However, FE models are very time consuming. Therefore, they are not recommended to be used with dynamic circuit analysis.

Analytical tools are a better solution than FE models concerning time computation. One of the tools is magnetic equivalent circuits (MECs) [12], [13]. MECs are faster than FE solvers with a moderate accuracy. However, MECs take time in building the network and need good knowledge in interpreting the flux paths. Analytical formulas presented in [14], [15] using winding function approach to estimate the machine inductances.

Electric circuit (EC) based model is a better solution when considering the dynamic analysis with the electric grid and the wind turbine mechanical [10]. They give a faster appealing result. DQ and ABC reference frame analysis of the machine are used in many literature [16]–[19]. However, the non-linearities existing in the machine are not considered in those analyses. The inductances in the EC model are assumed to be constant values. Moreover, from the electromagnetic field analysis, it can be shown that it is mandatory to include the effect of saturation on the machine inductances. Therefore, an accurate model includes a real time implementation of the machine inductance saturation is necessary for accurate machine modelling representation.

Studying the impact of saturation in a real time simulation for BDFRG is not presented up to date. However, implementing the inductance variation in real time simulation, has been performed by different methods in conventional machines like, make a live link between the Simulink model and FE model as presented in [20], this method takes a very long time to execute one cycle at each simulation stepping time. Other methods are usually used by generating a lookup table from the FE model and use it in the simulation model [8], [21] or by getting an analytical expression between currents and machine inductances [22], [23].

There are four contributions for this work. First, complete model of BDFRG is presented in FE including the effect of saturation. Second, the paper studies the effect of saturation on the generator inductances and performance for

all loading conditions with different modes of operations. Third, the purposed BDFRG real time simulation analytical model includes the inductance saturation by using a lookup table generated from the FE model, in this method, the computational time of the FE analysis is independent of the stepping time of simulation. Fourth, the developed BDFRG model has been implemented in wind energy system to achieve maximum power point and reactive power control.

The following sections of this paper are organized as follows. Section 2 presents the modelling of the BDFRG driving the wind turbine, including the mathematical analytical models, FE models, and the coupling between them. This includes the magnetic saturation effect. Section 3 presents the used control schematic. Section 4 covers the simulation results with the FE verification. Conclusions are presented in the final section.

II. BDFRG WIND ENERGY CONVERSION SYSTEM

This section presents the modelling of the wind turbine model, analytical model of the generator, FE model of the BDFRG, and coupling between the analytical equations and the lookup table generated from the FE models.

A. WIND TURBINE MODEL

The mechanical power could be extracted from the wind is given by [24]:

$$P_{mw} = 1/2\rho\pi R^2 C_p(\lambda_t, \beta)u_w^3 \tag{1}$$

where β is the blade pitch angle, λ_t is the tip-speed ratio, ρ is the air density, R is the turbine blade radius, u_w is the wind speed, and C_p is the wind power coefficient and the tip speed ratio can be expressed as:

$$\lambda_t = R\omega_{rm}/u_w \tag{2}$$

where, ω_{rm} is the mechanical rotor speed and the wind power coefficient C_p can be expressed as:

$$C_p(\lambda_t, \beta) = 0.5176\left(\frac{116}{\lambda_i} - 0.4\beta - 5\right)e^{-\frac{21}{\lambda_i}+0.0068\lambda_t}$$
$$\frac{1}{\lambda_i} = \frac{1}{\lambda_t + 0.08\beta} - \frac{0.035}{\beta^3 + 1} \tag{3}$$

B. BDFRG MODELLING

This section presents the generator mathematical modelling and FE model, to study the generator performance under different situations of loading conditions and explain the inductance variation effect.

1) ANALYTICAL DYNAMIC MODELLING

The following equations show the BDFRG dynamic equations in rotating reference frame [3]. The d and q axes primary induced fluxes λ_{pd} and λ_{pq} and the secondary d and q axes induced fluxes λ_{sd} and λ_{sq} can be expressed as:

$$\lambda_{pd} = L_p i_{pd} + L_{ps} i_{sd} \tag{4}$$
$$\lambda_{pq} = L_p i_{pq} + L_{ps} i_{sq} \tag{5}$$

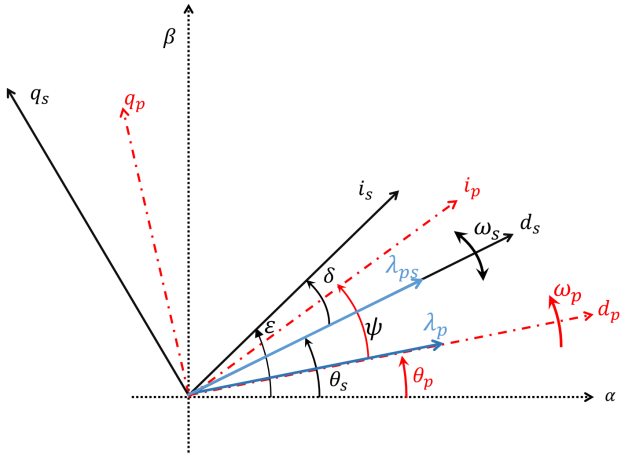

FIGURE 2. The arbitrary reference frames in d-q for primary and secondary windings.

$$\lambda_{sd} = L_s i_{sd} + L_{ps} i_{pd} \tag{6}$$
$$\lambda_{sq} = L_s i_{sq} + L_{ps} i_{pq} \tag{7}$$

where L_p, L_s and L_{ps} are the generator primary, secondary and mutual inductances, respectively, i_{pd} and i_{pq} are the primary d-q axes currents and i_{sd} and i_{sq} are the secondary d-q axes currents.

The primary d and q axes induced voltages v_{pd} and v_{pq}, and the secondary d and q axes induced voltages v_{sd} and v_{sq} are presented as:

$$v_{pd} = R_p i_{pd} + \frac{d\lambda_{pd}}{dt} - \omega_p \lambda_{pq} \tag{8}$$
$$v_{pq} = R_p i_{pq} + \frac{d\lambda_{pq}}{dt} + \omega_p \lambda_{pd} \tag{9}$$
$$v_{sd} = R_s i_{sd} + \frac{d\lambda_{sd}}{dt} + \omega_s \lambda_{sq} \tag{10}$$
$$v_{sq} = R_s i_{sq} + \frac{d\lambda_{sq}}{dt} - \omega_s \lambda_{sd} \tag{11}$$

where, ω_p and ω_s are the primary and secondary electrical angular velocities, respectively, and relation between them is given as:

$$\omega_r = p_r \omega_{rm} = \omega_p + \omega_s \tag{12}$$

where, ω_r and ω_{rm} are the generator electrical and mechanical angular velocities, respectively. The primary variables rotate with ω_p frame and the secondary variables rotate with ω_s frame, hence the variables appear as a DC in their frames. Fig. 2 shows the position relation between the primary and secondary reference frames, which is covered by:

$$\theta_r = p_r \theta_{rm} = \theta_p + \theta_s \tag{13}$$

The generator electromagnetic torque is expressed as:

$$T_e = (3p_r L_{ps}/2L_p)(\lambda_{pq} i_{sd} + \lambda_{pd} i_{sq}) \tag{14}$$

The generator inductances depend on the primary and secondary currents due to the iron parts saturation. FE analysis is a good tool to study and estimate the generator inductances

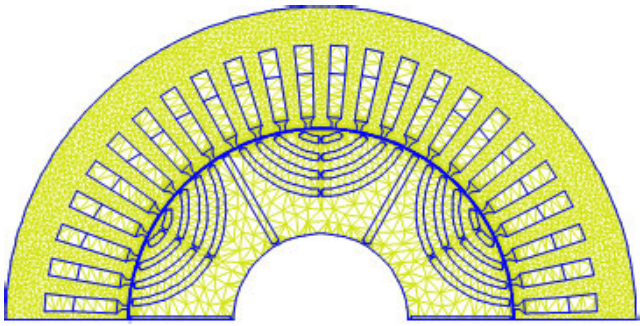

FIGURE 3. Half machine mesh modelling using FEMM software.

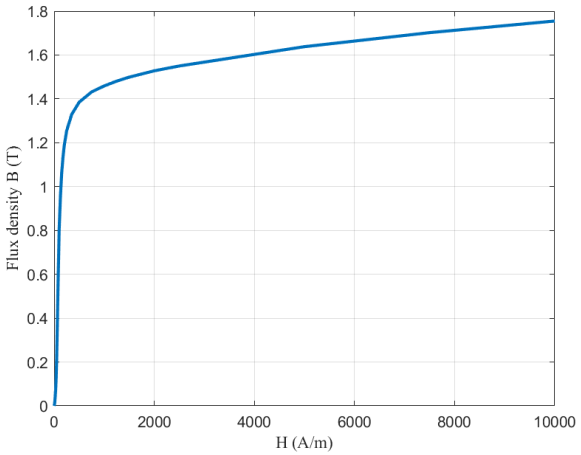

FIGURE 4. BH curve of M400-50A material used in modelling the stator and rotor parts.

TABLE 1. BDFRG prototype dimensions.

Parameter	Value
Stator Output Diameter	$235mm$
Stator internal diameter	$144mm$
Effective length	$70mm$
Number of stator slots	48 slot
Air gap length	$0.5mm$
Shaft diameter	$65mm$

using computational techniques by discretising the generator to smaller areas. The following section shows the generator FE modelling.

2) FINITE ELEMENT MODELLING

Estimating the generator inductances requires knowing the distribution of the electromagnetic fields in the generator parts. FEMM software is used to develop and study a model of 1 kW BDFRG. To decrease the computational time, only one half of the generator model is built using anti-periodic boundary condition [25]. Fig. 3 demonstrates one half of the machine modelling, where the stator slots consists of double layers, the primary winding distributed in the upper layer and the secondary winding distributed in the lower layer. The rotor is radially laminated with axial flux barriers. The dimensions of the used generator are given in table 1.

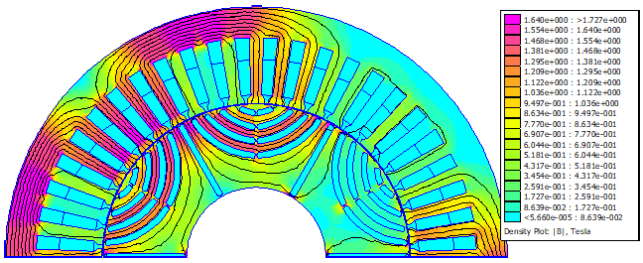

FIGURE 5. The flux density distribution at rated values of primary and secondary currents.

TABLE 2. BDFRG parameters and the turbine parameters.

BDFRG Parameters	Value
BDFRG Power	$1kW$
Rated voltage	$130V$
Max. speed	$1000rpm$
Poles (Prim, Sec., Rotor)	$8/4/6$poles
Rated Currents (I_{pm},I_{sm})(Max value)	3.07A, 3.23A
R_p, R_s	3.2Ω, 3.16Ω
L_p, L_s,and L_{ps}	$0.19H, 0.17H, 0.096H$
J_m	$0.2kg.m^2$
Turbine Parameters	
Rated power	$1kW$
Wind velocity range V_w	$3-13m/s$
V_{opt}	$8m/s$
Blade Radius	$1.6m$
λ_{opt}	7.31
Gear box ratio	1.8623

To include the core saturation, the BH curve of M400-50A material used in modelling the stator and rotor parts is presented in Fig. 4. The resultant flux density distribution of the FEMM model at rated values of primary and secondary currents listed in table 2, is shown in Fig. 5. By examination of Fig. 5, it is appearing that a large part the core is saturated according to the BH curve shown in Fig. 4 and the stator teeth and the rotor flux paths have an average flux density of about 1.5T.

The FEMM model is run at different values of primary and secondary currents up to 3 times the rated values with the help of MATLAB m-file. The resulted relationship between inductances and primary currents are illustrated in Fig. 6. It can be observed that the inductances are remarkably decreased with currents specially at high values of currents, and the inductances may decrease to half the considered constant values listed in table 2.

3) COUPLING BETWEEN FEMM AND SIMULINK MODEL

To consider the iron parts saturation in real time simulation, a live-link has been developed between FEMM software and MATLAB model is presented in the following section.

Live-link between MATLAB m-files and the FEMM software [26] is built to allow the extraction of the electromagnetic characteristics with different rotation angles and currents. The inputs of the FE models are the d and q axes currents, and the generator rotation is done by static steps. Fig. 7 shows the rotor position at a cretin step of

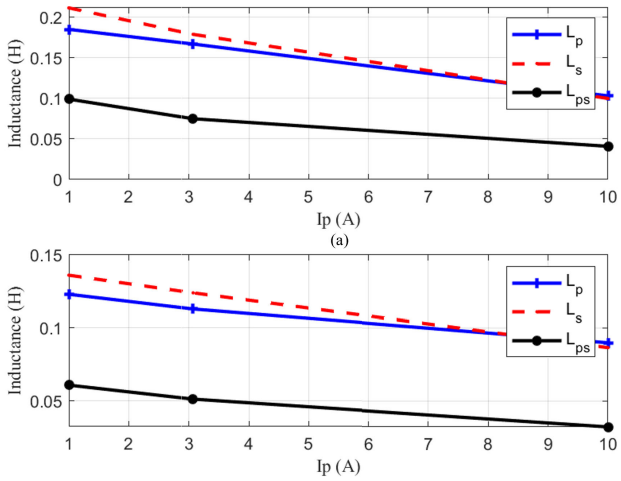

FIGURE 6. The change of the generator inductances (L_p, L_s and L_{ps}) vs primary currents (a) $I_{sm} = 3.23A$, (b) $I_{sm} = 10A$.

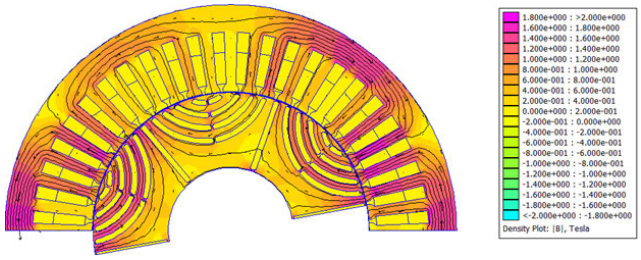

FIGURE 7. The rotor rotation using static steps.

the rotor rotation. The outputs of the FE model are the d and q axes primary and secondary fluxes. Equations (5) to (7) are used to extract the primary, secondary, and mutual inductances.

To generate the lookup table, the FE model is solved at different values of primary currents, secondary currents and different values of current angles (i.e α_p,α_s) where $\alpha_p = tan^{-1}(I_{pq}/I_{pd})$and $\alpha_s = tan^{-1}(I_{sq}/I_{sd})$. The grid data for different d and q axes primary and secondary currents are generated up to 10A. This ensures that the generator is heavily saturated.

A for-loop MATLAB m-file is performed with changing the primary and secondary currents with 3 discretization (1, 3.23, *and* 10 A), and the current angles with 8 discretization from zero to 2π. The number of grid points equal $9 * 64$ points. The inductance values are generated and recorded in a 4-D lookup table. The computational time to execute one run take about 3 days using Intel®Core i7-3370 CPU @3.40GHz, 8GB RAM desktop. Sample of the lookup table results at constant values of primary currents, secondary currents, and different angles of α_p and α_s is summarized in Fig. 8.

Fig. 8(a) shows that the primary inductance changes form 0.195 H to 0.161 H with $+2\%$ to -15.7% of the constant primary inductance value are given in table 2. In Fig. 8(b), the secondary inductance changes form 0.17H to 0.218H with 0

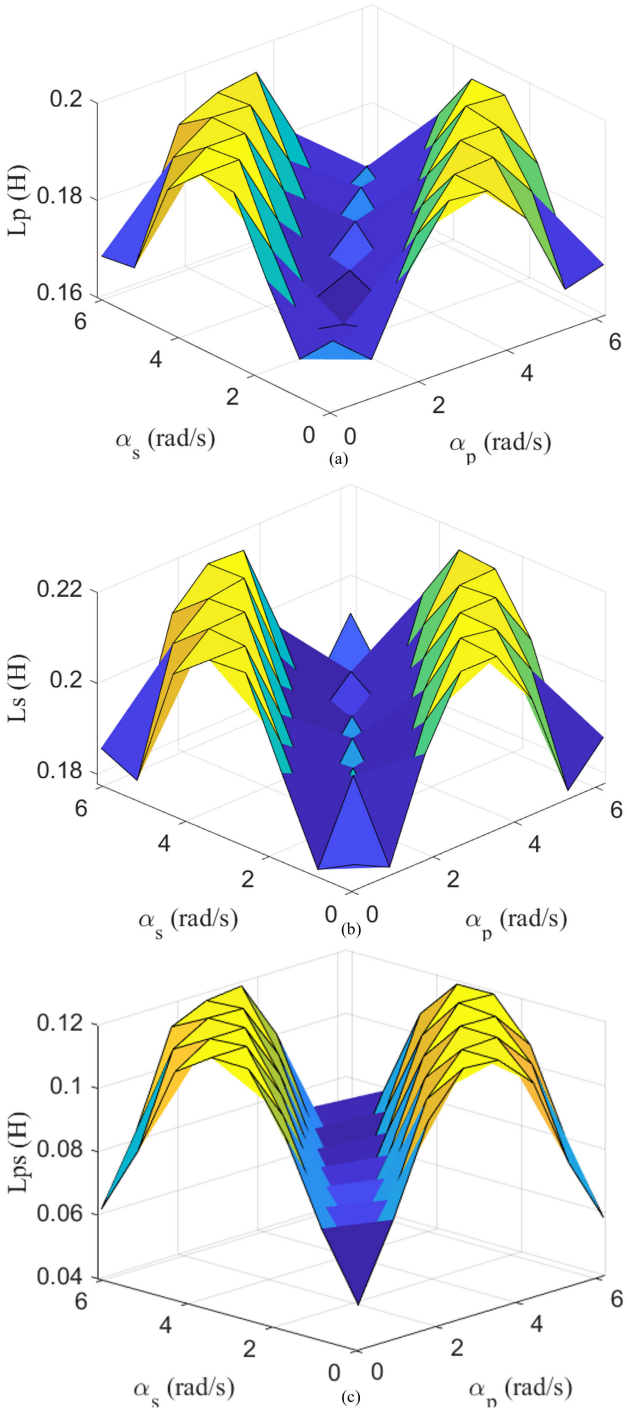

FIGURE 8. The lookup table outputs (generator inductances) at different values of d-q axes currents. (a) L_p, (b) L_s, (c) L_{ps}.

to 28% of the constant inductance value, also the change of mutual inductance is 0.04 H to0.12 H with -50% to 25% as shown in Fig. 8(c). It is known that the mutual inductance is directly proportional to the generator torque (back to (14)), so 50% change in the generator torque is a noticeable value, hence using constant generator inductances in simulation will affect badly on the generator performance when compared to experimental results.

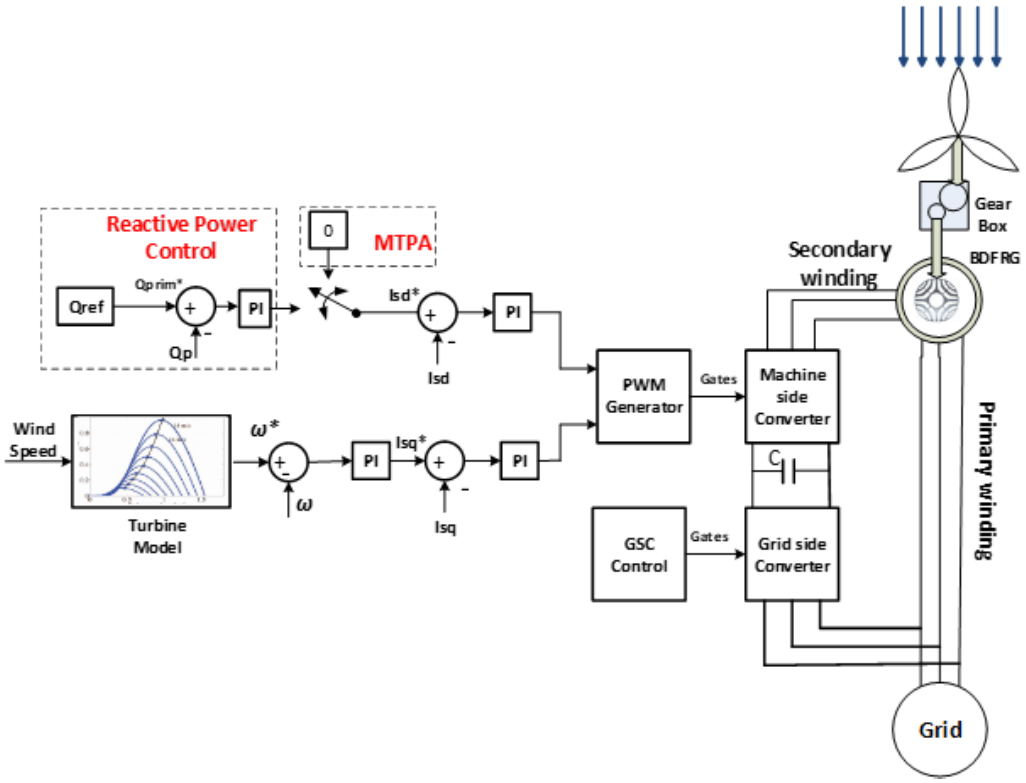

FIGURE 9. The control procedure of generator side converter.

III. CONTROL SCHEME

The primary of the BDFRG is directly connected to the grid and the secondary is connected to grid via grid side converter and generator side converter to control the active and reactive power to/from the grid. Basically, the control techniques tune the d-q currents of the secondary winding to control the total active and reactive power.

The grid side converter control is used to adjust active and reactive power from BDFRG to the grid and maintain the DC bus voltage at a constant value, by controlling the d-q axes grid currents [10]. On the other hand, the generator side converter is used to obtain the maximum power from the wind turbine and to control the total power factor of the generator [27]. Many control techniques introduced in literature with BDFRG to meet the grid requirements of controlling the generator output active and reactive power [28]–[31]. Field-oriented control (FOC) is a prime technique used in decoupling the active and reactive power. Therefore, FOC is used in this paper to control the generator side converter.

The total active power (P_{tot}) of the generator and hence the torque can be computed from (15). The primary angle (θ_p) is generated using the phase locked loop (PLL), so that the d-axis primary voltage equals to zero. According to FOC alignment of λ_{pd} with d_p axis will result in $\lambda_{pq} = 0$ and $\lambda_p = \lambda_{pd}$. Hence, from (15), the primary active power is directly proportional to secondary quadrature current i_{sq} (λ_p is constant as the primary winding connected to the grid bus). Therefore, by controlling the i_{sq}, the generator torque can be easily controlled.

In addition to the active power control, the reactive power of the primary side can also be regulated by controlling the secondary d-axis current (i_{sd}). The value of i_{sd} can be driven from the reference desired reactive power (Q_{ref}) given in (16), or by setting $i_{sd} = 0$ when the generator operates with maximum torque per secondary current MTPA approach [31].

$$P_{tot} = T_e \omega_{rm} = \frac{3 p_r L_{ps} \omega_{rm}}{2 L_p} \left(\lambda_{pq} i_{sd} + \lambda_{pd} i_{sq} \right) \quad (15)$$

$$Q_p = \frac{3}{2} \frac{1}{L_p} \omega_p \lambda_{pd} \left(\lambda_{pd} - L_{ps} i_{sd} \right) \quad (16)$$

The optimum speed of the wind turbine system depends on the optimum value of the tip speed ratio (λ_{opt}) and the measured wind speed (u_w). Therefore, there are two loops of control. One is used to control the speed and the inner loop is used to control the q-axis current. Fig. 9 shows the control schematic diagram of the system.

IV. SIMULATION RESULTS AND DISCUSSION

The grid connected BDFRG wind turbine model is used to study the generator behaviour under the wind speed variation. The wind speed range is selected from 4 m/s to 8 m/s to cover the generator modes of operations in sub-synchronous and super-synchronous modes.

To take into consideration the effect of the saturation, two different models of the BDFRG are used. In the first

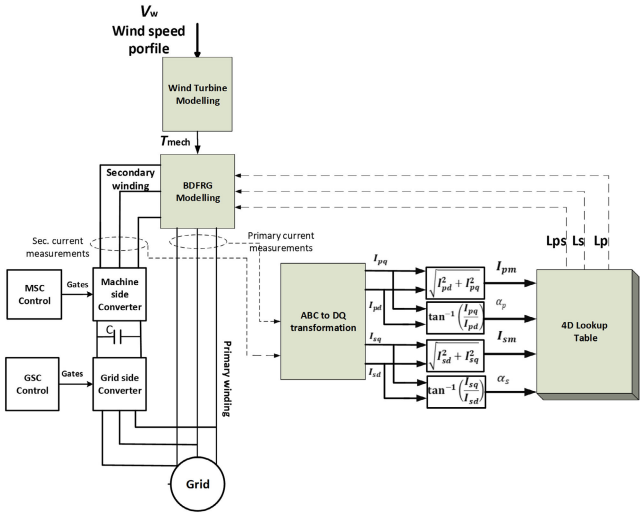

FIGURE 10. System schematic block diagram.

model, the values of inductances (L_p, L_s, and L_{ps}) are assumed constant as given in table 2. while in the second model, the values of the inductances are variable based on the lookup table generated from the FE model described in section 2. The inductances in this case are function of the current magnitudes (I_{pm},I_{sm}) and the current angles of the primary α_p and secondary α_s, therefore the inductances in the generator modelling equation can be rewritten as ($L_p(I_{pm}, I_{sm}, \alpha_p, \alpha_s)$, $L_s(I_{pm}, I_{sm}, \alpha_p, \alpha_s)$, $L_{ps}(I_{pm}, I_{sm}, \alpha_p, \alpha_s)$). The whole system simulation block diagram including the lookup table is shown in Fig. 10.

A comparison between the results of the two models is obtained to study the effect of saturation in normal operation. The simulations are implemented with MTPA approach and the reactive power control strategy. Results are measured at steady state, where at each wind speed the simulations are performed till the steady state is reached and then the results are recorded.

A. MTPA RESULTS

In case of MTPA operation, i_{sd} is set to be zero and i_{sq} is regulated from the reference wind speed to obtain the maximum power form wind speed. Fig. 11 shows the generator d-q primary and secondary currents at different wind speeds, with the two cases of constant and variable inductances. The calculations of inductances using the lookup table reveal a marginal difference to the constant inductance results especially for the direct component of the primary current, in consequence of saturation.

Fig. 12 depicts the ability of the proposed control to trace maximum power point. Basically, the difference between the developed power and the output power shown in Fig. 12 due to the copper losses, on the other hand, a small difference occurred in output power calculation between the use of constant inductance and variable inductance models. The difference is more notable in super-synchronous speeds

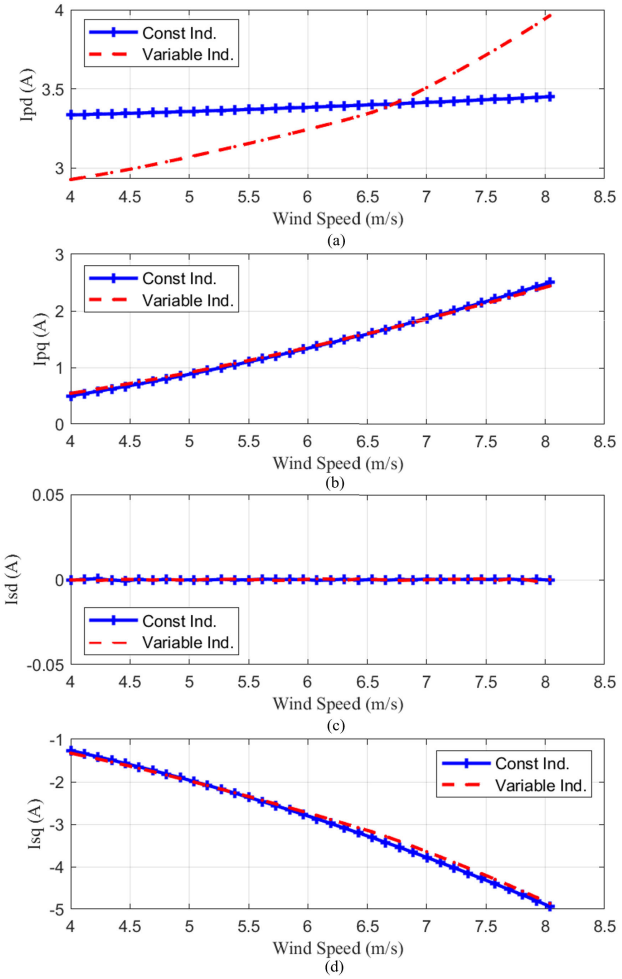

FIGURE 11. The generator d-q current results in case of constant and variable inductance, (a) the primary d-axis current, (b) the primary q-axis current, (c) the secondary d-axis current, (d) the secondary q-axis current.

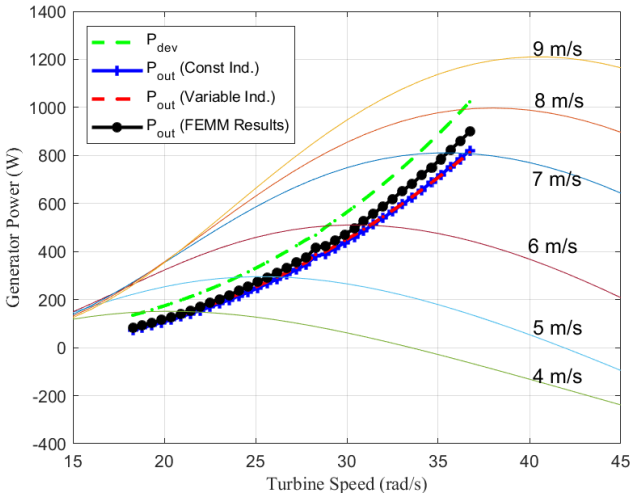

FIGURE 12. Generator power in case of MTPA control.

(synchronous speed 500 *rpm* at 6.15 *m/s*) as a result to the high values of currents and inductance saturation.

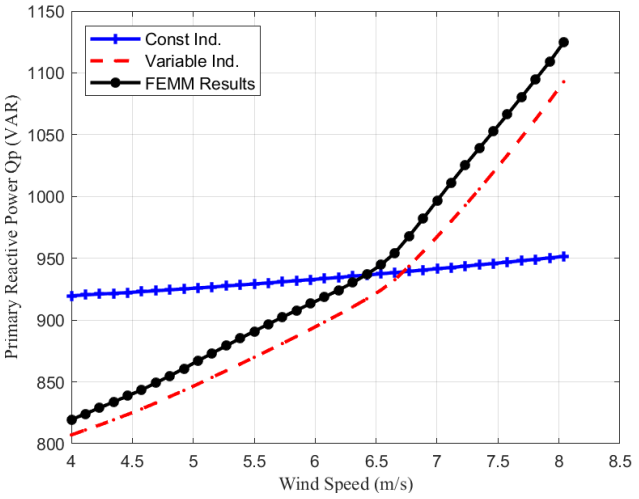

FIGURE 13. Generator reactive power factor in case of MTPA control.

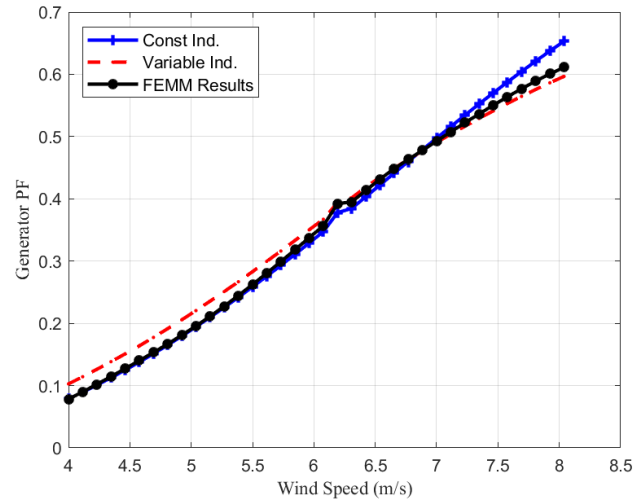

FIGURE 14. Generator power factor in case of MTPA control.

The FE analysis presented in [7] gives good agreement between the experiments and the simulation results. Therefore, the FEMM model is used to verify the lookup table validity, through an active link between the MATLAB m-file and the FEMM model [26]. The FEMM model is performed for each wind speed (with the values of primary and secondary currents recorded from the variable inductance case) and the FEMM results are compared with the generator simulation results at each wind speed.

The generator primary reactive power Q_p is shown in Fig. 13. At high values of wind speeds, i.e. the currents become high, the difference in Q_p becomes noticeable between the constant and variable inductance models. This is a consequence of the saturation on the value of L_p. Back to (16) with a fixed value of λ_{pd} and $i_{sd} = 0$, this results that Q_p is inverse proportional to L_p.

Fig. 14 presents the generator power factor at different wind speeds for the three models, a small difference occurs at super-synchronous speeds as expected. The inductances

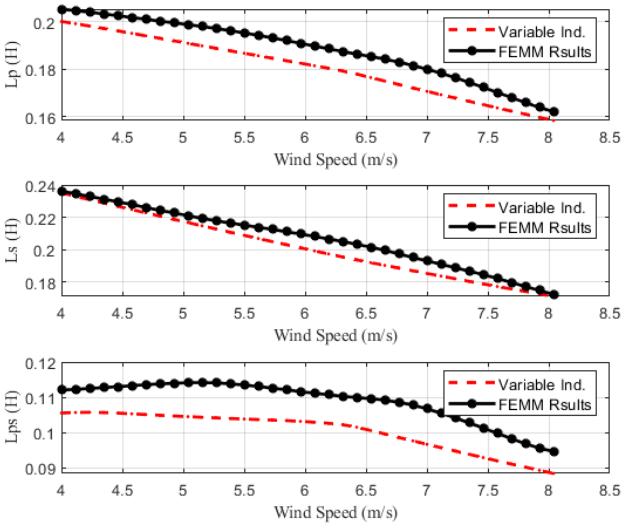

FIGURE 15. Generator inductances at different values of wind speed L_p, L_s and L_{ps} respectively vs primary currents.

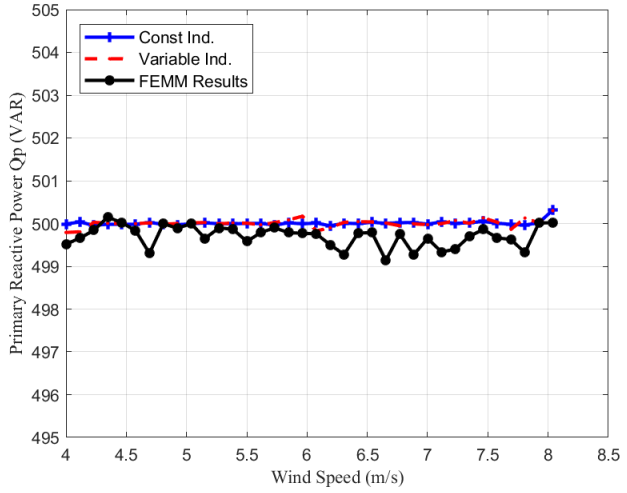

FIGURE 16. Generator Primary reactive power in case of reactive power control.

generated from the lookup table during simulation are compared with that obtained from FEMM at same values of currents and they are shown in Fig. 15.

Comparing the simulation results with the FEMM results to test the lookup table validity. Figs. 12-15 reveal a partial agreement in results, which can be treated by increasing the number of points used to run the lookup table and hence, get a detailed lookup table.

B. REACTIVE POWER CONTROL RESULTS

The two models are simulated to adjust the generator's reactive power at a constant value of ($Q_p = 500VAR$) at different wind speeds in the cases of constant and variable inductances. Moreover, the FEMM model is used to validate the variable inductance model. Fig. 16 shows the primary reactive power at different wind speeds for the three models.

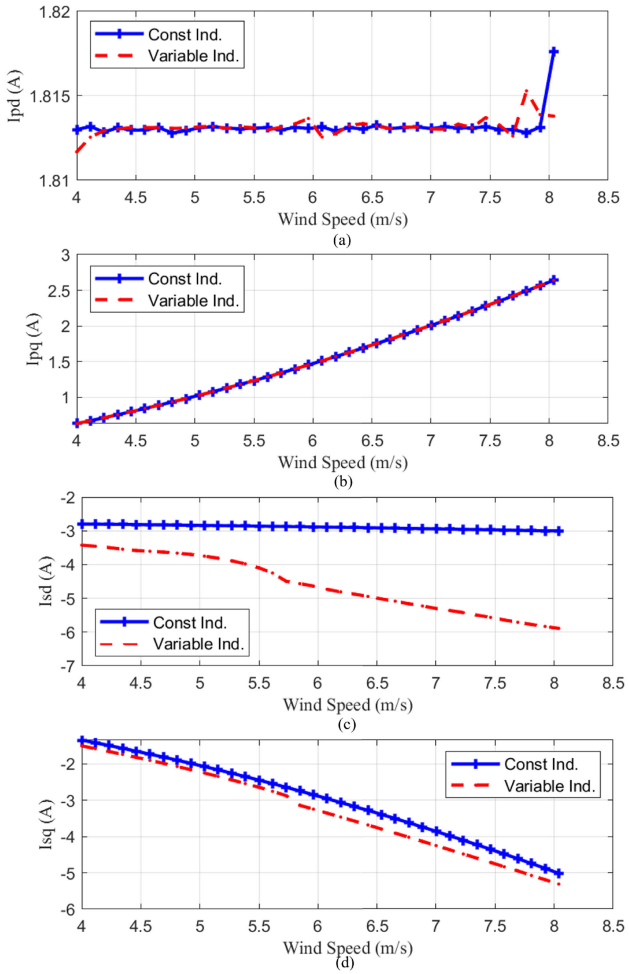

FIGURE 17. Generator d-q primary and secondary currents with reactive power control.(a) the primary d-axis current, (b) the primary q-axis current, (c) the secondary d-axis current, (d) the secondary q-axis current.

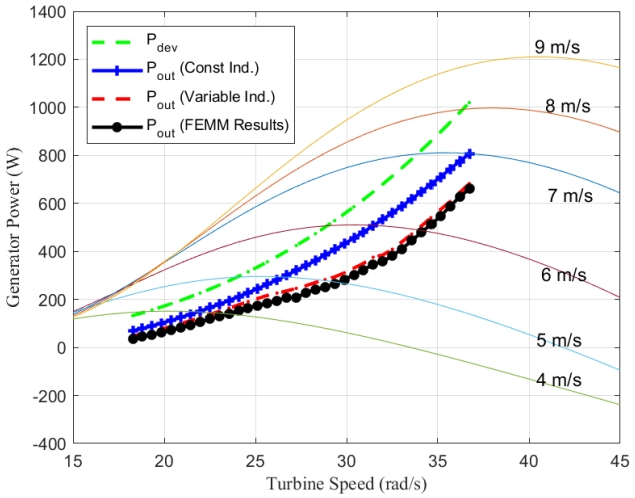

FIGURE 18. Generator power in case of reactive power control.

Fig. 17 shows the generator d-q primary and secondary currents at different wind speeds in case of variable inductances. The notable differences in the secondary

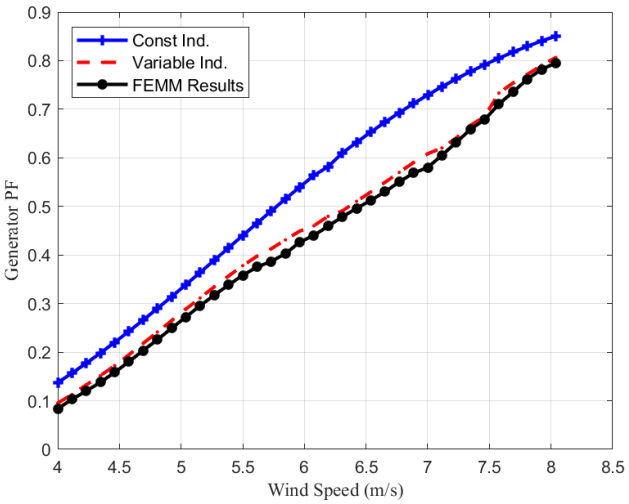

FIGURE 19. Generator power factor in case of reactive power control.

d-q currents between the two models are shown in Figs. 17 (c and d). There are notable differences in the controller performance between the two models at wind speeds higher than 5.8 m/s, due to the increase of saturation.

Fig. 18 depicts the difference of output generator power of variable inductance model (at super-synchronous speeds) dropped to more than 30 % of the output power in case of constant inductance, due to the increase of the copper power losses. The saturation effect is clearly observed in the generator power factor as shown in Fig. 19.

V. CONCLUSION

Brushless doubly fed reluctance generators (BDFRGs) real time modelling can be done using the assumption of linear inductances assuming the BH characteristics of the machine is linear. However, in this paper, it is proven out that inclusion of the inductance relationship with the currents give more accurate results.

A direct link between the Simulink model of the BDFRGs, driven wind turbine system, and the finite elements using FEMM software is developed via a lookup table. This lookup table is generated via the FEMM software. It relates the inductances of the machine with the input currents. Afterwards, this lookup table is included in the Simulink model. Different investigations are carried out to show the importance of the inclusion of the material non-linearities.

Comparable study between the effect of constant inductance and the lookup table is studied. It is done with the maximum torque per ampere (MTPA) and the reactive power control. It shows that with the reactive power control, the output power difference between the constant and variable inductances reaches 30% at some points. Therefore, it is important to include the non-linearity of the material. Notable differences between the two models can be observed in the power factor, output power and output currents of the machine. At the end, the variable inductance Simulink model is verified using the FEMM software. Lastly, the inclusion

of inductance current variation in the generator modeling is very important for accurate generator representation and more precise control performance in normal and abnormal conditions studies.

REFERENCES

[1] M.-F. Hsieh, Y.-H. Chang, and D. G. Dorrell, "Design and analysis of brushless doubly fed reluctance machine for renewable energy applications," *IEEE Trans. Magn.*, vol. 52, no. 7, pp. 1–5, Jul. 2016.
[2] F. Liang, L. Xu, and T. Lipo, "D-q analysis of a variable speed doubly AC excited reluctance motor," *Electr. Mach. Power Syst.*, vol. 19, no. 2, pp. 125–138, Mar. 1991, doi: 10.1080/07313569108909511.
[3] R. E. Betz and M. G. Jovanović, "Introduction to the space vector modeling of the brushless doubly fed reluctance machine," *Electr. Power Compon. Syst.*, vol. 31, no. 8, pp. 729–755, 2003.
[4] A. M. Knight, R. E. Betz, and D. Dorrell, "Design and analysis of brushless doubly fed reluctance machines," *IEEE Trans. Ind. Appl.*, vol. 49, no. 1, pp. 3128–3135, 2011.
[5] R. E. Betz and M. G. Jovanovic, "The brushless doubly fed reluctance machine and the synchronous reluctance machine—A comparison," *IEEE Trans. Ind. Appl.*, vol. 36, no. 4, pp. 1103–1110, Aug. 2000.
[6] S. Tohidi, P. Tavner, R. McMahon, H. Oraee, M. R. Zolghadri, S. Shao, and E. Abdi, "Low voltage ride-through of DFIG and brushless DFIG: Similarities and differences," *Elect. Power Syst. Res.*, vol. 110, pp. 64–72, May 2014. [Online]. Available: https://www.sciencedirect.com/science/article/pii/S0378779614000042
[7] D. Gay, R. E. Betz, D. Dorrell, and A. Knight, "Brushless doubly fed reluctance machine testing for parameter determination," *IEEE Trans. Ind. Appl.*, vol. 55, no. 3, pp. 2611–2619, May 2019.
[8] K. Yahia, D. Matos, J. O. Estima, and A. J. M. Cardoso, "Modeling synchronous reluctance motors including saturation, iron losses and mechanical losses," in *Proc. Int. Symp. Power Electron., Electr. Drives, Autom. Motion*, Jun. 2014, pp. 601–606.
[9] P. Han, M. Cheng, S. Ademi, and M. G. Jovanovi, "Brushless doubly-fed machines: Opportunities and challenges," *Chin. J. Electr. Eng.*, vol. 4, no. 2, pp. 1–17, 2018.
[10] O. Sadeghian, S. Tohidi, and B. Mohammadi-Ivatloo, "A comprehensive review on brushless doubly-fed reluctance machine," *Sustainability*, vol. 13, no. 842, pp. 1–39, 2021.
[11] A. C. Ferreira and S. Williamson, "Time-stepping finite-element analysis of brushless doubly fed machine taking iron loss and saturation into account," *IEEE Trans. Ind. Appl.*, vol. 35, no. 3, pp. 583–588, May 1999.
[12] M. F. Hsieh, I. H. Lin, and D. G. Dorrell, "Magnetic circuit modeling of brushless doubly-fed machines with induction and reluctance rotors," *IEEE Trans. Magn.*, vol. 49, no. 5, pp. 2359–2362, May 2013.
[13] M.-F. Hsieh, I.-H. Lin, and D. G. Dorrell, "An analytical method combining equivalent circuit and magnetic circuit for BDFRG," *IEEE Trans. Magn.*, vol. 50, no. 11, pp. 1–5, Nov. 2014.
[14] P. Han, J. Zhang, and M. Cheng, "Analytical analysis and performance characterization of brushless doubly fed machines with multibarrier rotors," *IEEE Trans. Ind. Appl.*, vol. 55, no. 6, pp. 5758–5767, Nov. 2019.
[15] P. Han, J. Zhang, and M. Cheng, "Theoretical and experimental investigation of the brushless doubly-fed machine with a multi-barrier rotor," in *Proc. IEEE Energy Convers. Congr. Expo. (ECCE)*, Sep. 2018, pp. 4964–4971.
[16] T. Taluo, L. Ristic, and M. Jovanovic, "Performance analysis of brushless doubly fed reluctance machines," in *Proc. 20th Int. Symp. Power Electron. (Ee)*, Oct. 2019, pp. 1–6.
[17] K. Kiran, S. Das, and A. Sahu, "Sensorless speed estimation and control of brushless doubly-fed reluctance machine drive using model reference adaptive system," in *Proc. IEEE Int. Conf. Power Electron., Drives Energy Syst. (PEDES)*, Dec. 2016, pp. 1–6.
[18] M. R. Agha Kashkooli and M. G. Jovanović, "Sensorless adaptive control of brushless doubly-fed reluctance generators for wind power applications," *Renew. Energy*, vol. 177, pp. 932–941, Nov. 2021. [Online]. Available: https://www.sciencedirect.com/science/article/pii/S0960148121008430
[19] M. G. Mousa, S. M. Allam, and E. M. Rashad, "Sensored and sensorless scalar-control strategy of a wind-driven BDFRG for maximum wind-power extraction," *J. Control Decis.*, vol. 5, no. 2, pp. 209–227, Apr. 2018.
[20] F. D'hulster, K. Stockman, and R. J. M. Belmans, "Modelling of switched reluctance machines: State of the art," *Int. J. Model. Simul.*, vol. 24, no. 4, pp. 216–223, 2005.
[21] P. C. Palavicino and B. Sarlioglu, "Prediction of failure path current for synchronous reluctance and interior permanent magnet synchronous machines accounting for saturation," in *Proc. IEEE Transp. Electrific. Conf. Expo (ITEC)*, Jun. 2020, pp. 1165–1170.
[22] T. Fukami, M. Momiyama, K. Shima, R. Hanaoka, and S. Takata, "Steady-state analysis of a dual-winding reluctance generator with a multiple-barrier rotor," *IEEE Trans. Energy Convers.*, vol. 23, no. 2, pp. 492–498, Jun. 2008.
[23] C. Ogbuka, C. Nwosu, and G. Umoh, "A new cross-saturated torque model of highly utilized synchronous reluctance machine," *Arch. Electr. Eng.*, vol. 67, no. 1, pp. 109–121, 2018.
[24] M. Cheng and Y. Zhu, "The state of the art of wind energy conversion systems and technologies: A review," *Energy Convers. Manage.*, vol. 88, pp. 332–347, Dec. 2014.
[25] I. Storozhenko and Q. Sun, "Numerical modeling of a wind turbine based on the doubly-fed induction generator topology," Tech. Rep., 2017.
[26] A. Jeklin. (2016). *Finite Element Method Magnetics*. [Online]. Available: http://www.femm.info/wiki/NewBuild
[27] G. S. Meera and N. A. Divya, "Rotor side converter control of DFIG based wind energy conversion system," *Int. J. Eng. Res.*, vol. V4, no. 8, pp. 607–612, Aug. 2015.
[28] M. Kumar and S. Das, "Model reference adaptive system based sensorless speed estimation of brushless doubly-fed reluctance generator for wind power application," *IET Power Electron.*, vol. 11, no. 14, pp. 2355–2366, Nov. 2018.
[29] M. Jovanović, S. Ademi, and J. K. Obichere, "Comparisons of vector control algorithms for doubly-Fed reluctance wind generators," in *Transactions on Engineering Technologies*. Dordrecht, The Netherlands: Springer, Jul. 2015.
[30] M. Moazen, R. Kazemzadeh, and M.-R. Azizian, "Model-based predictive direct power control of brushless doubly fed reluctance generator for wind power applications," *Alexandria Eng. J.*, vol. 55, no. 3, pp. 2497–2507, Sep. 2016. [Online]. Available: https://www.sciencedirect.com/science/article/pii/S1110016816302137
[31] E. F. Yassin, H. M. Yassin, and M. M. Hallouda, "Control strategies for brushless doubly fed reluctance generator in WECS: Review," in *Proc. IEEE Int. Conf. Power Eng. Appl. (ICPEA)*, Mar. 2021, pp. 79–84.